Wind-Induced Currents and Bottom-Trapped Waves in the Santa Barbara Channel

GUILLERMO AUAD, MYRL C. HENDERSHOTT, AND CLINTON D. WINANT

Center for Coastal Studies, Scripps Institution of Oceanography, La Jolla, California

(Manuscript received 19 November 1996, in final form 5 June 1997)

ABSTRACT

The Santa Barbara Channel (SBC) is a coastal basin about 100 km long bounded by the Southern California mainland on the north and by a chain of islands on the south. The SBC is at most 50 km wide and just over 600 m deep. The nature of current and wind variance peaks in the 2–4-day and 4–6-day bands in the channel are analyzed from January to July 1984. For both bands the dominant empirical mode of the currents is highly coherent with the dominant empirical mode of the winds over this region. Surface intensification of currents is revealed by measurements made between 25 and 300 m. In contrast the deeper currents are characterized by bottom trapping. Evidence for baroclinic bottom-trapped topographic Rossby waves is found on the northern shelf at the western mouth of the channel in both frequency bands. At 30 m the distribution of phases shows currents at the center of the western mouth leading the southern interisland passes by about 0.3 day and the eastern mouth by about 0.6 day. In both bands co- and quadrature vectors of currents and winds describe this wind–current system in detail. It is speculated from spatial and temporal eigenfunctions of currents and winds and from available satellite images that the dominant current mode described above is a channelwide response to upwelling north of Point Conception (northwestward of the SBC). The upwelling-related currents cause a net inflow of mass into the western end of the channel, which is compensated by an outflow passing through both the interisland passes and through the eastern mouth of the channel. As a result of the narrowness and shallowness of the passes and of the shallowness of the southern shelf in general, high flow speeds are attained there that, the authors speculate, seem to force deep high-frequency motions both at the center of the SBC and at the northern half of its western mouth.

1. Introduction

The Santa Barbara Channel (SBC) is located between the Southern California coastline and a chain of offshore islands. The channel is roughly 100 km long and 40–50 km wide with a maximum depth just over 600 m (Fig. 1). The channel is separated from the Santa Monica Basin to the east by a sill beneath 200 m at the eastern entrance and from Arguello Canyon to the west by a sill about 500 m deep at the western entrance.

Brink and Muench (1986) have reported direct observations of currents, with emphasis on the upper-layer circulation, based on a combination of results from the OPUS (Organization of Persistent Upwelling Structures) Experiment and observations from a pilot study conducted in 1983 by the Minerals Management Service (MMS) in the SBC. Between Points Arguello and Conception (northwest of the SBC), they observed wind-driven upwelling events in both mean and fluctuating flows. They conclude that the time-varying currents in the SBC were not clearly related to local winds but were, rather, apparently associated with larger-scale meteorological patterns. In the present paper, the channel response to local winds is investigated in more detail by combining two different filtering techniques, that is, band passing and empirical orthogonal decomposition (EOF) (Wallace and Dickinson 1972). These procedures can be very useful when trying to isolate a given signal from datasets that compromise multiple physical processes with comparable amounts of variance. The wind and current results from the SBC exemplify such a dataset because of the low but significant wind–current correlations and sea level–current correlations estimated by Brink and Muench (1986).

Confirming these latter results, low wind–current correlations are also found in Auad (1996, hereafter A96), who analyzes the 1984 dataset. In his work, A96 finds that, even though the wind outside the channel's western entrance during the upwelling season is at least as energetic as in the CODE area, the physical geometry, the wind gradients, and that in the SBC the mean winds blow in the opposite sense to the mean currents (e.g., Brink and Muench 1986; Gunn et al. 1987; A96) may contribute, among other things, to the lower wind–current correlations found in the SBC.

Although Brink and Muench gave little attention to the deep circulation in the SBC, Gunn et al. (1987) reported results from one year of moored current meter

Corresponding author address: Dr. Guillermo Auad, Climate Research Division, Scripps Institution of Oceanography, UCSD, La Jolla, CA 92093-0224.
E-mail: guillo@ucsd.edu

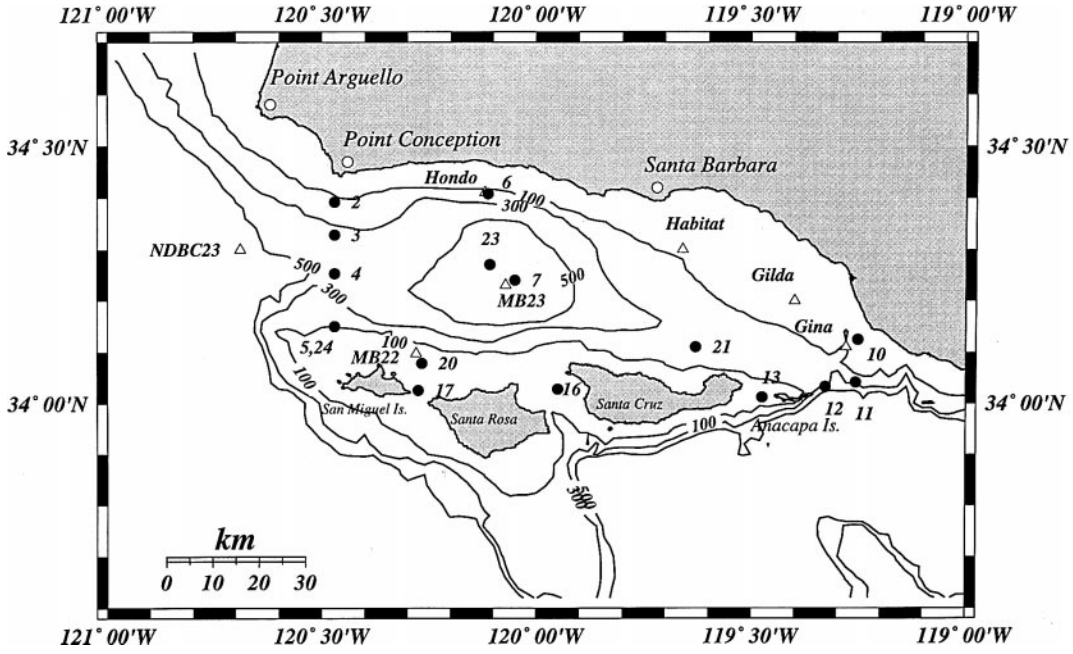

FIG. 1. Bottom topography (0-m, 100-m, 300-m, and 500-m contours) and mooring locations of the Santa Barbara Channel and surrounding areas. Circles correspond to current meters and triangles to wind stations.

observations in the SBC carried out by the MMS in 1984 and noted that the deepest current meters in this dataset show strong high-frequency (period of a few days) oscillations. Their speculation that these could be a manifestation of the bottom-trapped baroclinic waves, first solved for by Rhines (1970), is examined in detail in the present paper. In their report Gunn et al. also show the low-passed vector time series at the passes between the channel islands (southern bound of the SBC). These records are also dominated by oscillations with a period of a few days but with much larger amplitudes than the ones seen at the deepest current meters located at the western entrance and at the center of the channel. A possible connection between currents on the southern shelf (interisland passes included) and currents in the deep SBC is also investigated here.

In a rather different approach, Lagerloef and Bernstein (1988) use Advanced Very High Resolution Radiometer (AVHRR) images of sea surface temperature to study the surface temperature patterns in the SBC during 1984. Through empirical orthogonal analysis they find two different signals, a quarter of a period out of phase, with annual frequency. The first one is characterized by a thermal front running NW–SE across the channel; the other one is approximately homogeneous in space throughout the channel. This later mode has minimum temperature in late May and maximum in mid-September.

Auad and Hendershott (1997) and A96 show that the SBC has a complicated flow field where there is not one single component of the flow that dominates over the others—hence the need to study this complex system by parts. In this article, we only deal with the wind-driven component of the flow and the analysis will be concentrated in those frequency bands where both currents and winds show maximum variance, namely, the 2.0–4.0- and 4.0–6.0-day bands. We believe that the wind-induced currents should have an important contribution to the total flow since, as reported by Dorman and Winant (1995) in an analysis of buoy data for the period 1981–1990, the western half of the SBC is the area of strongest seasonal wind forcing along the U.S. West Coast.

In summary, the goals of this paper are to (i) isolate the locally wind-driven currents in the SBC, (ii) qualitatively and quantitatively describe the wind-induced currents inside the channel, and (iii) offer some speculations about the physical processes involved in the generation of the wind-induced currents.

The paper is organized as follows: in section 2 selected observations of currents and winds are presented in both time and frequency domains. Preliminary evidence of a channel-coherent pattern and of wind-driven currents is shown in this section. In section 3, the wind-driven part of the currents is isolated and described, and it will show to have a complicated spatial structure in both 2.0–4.0- and 4.0–6.0-day bands. Both near-surface and near-bottom currents are studied. Although part of the same mode, the near-surface and bottom wind-induced currents are shown to have different dynamics: the near-surface currents are very likely associated to upwelling-generated equatorward currents, while the

TABLE 1. Instrument, mooring, and relief information. The location of each mooring is shown in Fig. 1. Depths are in meters, and isobath orientations, in degrees, are relative to the east direction. The ''Relief'' columns include both the total bottom depth (H) in meters and the estimated isobath orientation (O) in degrees relative to east.

Instrument		Relief	
ID	Depth (m)	H	O
			−16
021	30	150	
022	100		
031	30	366	−6
032	200		
033	350		
041	30	476	−15
042	100		
043	250		
051	30	90	−11
052	65		
061	30	150	−3
062	100		
071	30	563	−3
073	538		
111	30	300	32
112	80		
113	150		
121	30	98	−140
122	80		
161	25	44	−65
172	28	33	−122
201	30	73	180
202	65		
211	30	183	−7
212	80		

bottom currents are interpreted as bottom-trapped baroclinic Rossby waves. Section 4 is left for discussions and section 5 summarizes the findings of this article.

2. The observations

a. The data in the time domain

The observations used in this analysis are described in detail by Gunn et al. (1987) and A96. Thirty Aanderaa current meters were arrayed on 14 moorings, recording current amplitude and direction every 30 minutes. In addition, wind observations were reported hourly from 6 fixed stations. The mooring and wind station locations along with the mooring ID are shown in Fig. 1, while Table 1 shows the mooring and instrument depths. Mooring IDs were kept identical to those given by Gunn et al. (1987) in order to facilitate comparison with their work. Each mooring is assigned a two digit ID number. Each current meter is assigned a three digit number. The first two digits correspond to the mooring where this current meter belongs; on a given mooring, different current meters are identified by the third digit, which increases with increasing depth. Thus, the shallower instrument on mooring 02 is identified as 021, the next one deeper as 022, etc. The measurements extended from January 1984 to January 1985, but the present study is restricted to the period January 1984 to July 1984 because this period has a much more complete coverage, in both space and time, of the currents in the channel. Of the 30 records available, 5 were not used in the analysis presented here because they were appreciably shorter than five months. During this time, winds are stronger than during the second half of the year.

Figure 2 shows selected time series after low-passing with the pl64 filter (Limeburner 1985) having a cutoff period of 38 h. It is seen that both at the passes (current meters 161 and 172) and in the deep SBC (current meters 033 and 073) high-frequency fluctuations (period of a few days) dominate the records. The winds differ between the channel (e.g., Habitat) and regions bordering it (buoy NDBC23). A strong south-to-southeastward mean dominates the record at NDBC23, while at Habitat winds are weaker with an almost eastward mean. Note that after about 10 May there is a decrease of the wind velocity amplitude at Habitat, and simultaneously there is an increase of the mean (into the channel) flow at the pass moorings 16 and 17. Brink and Muench (1986) also noted that there is an important change in the channel currents in May 1983.

b. The data in the frequency domain

The velocity records of instruments 032, 033, 043, 073, 212, 161, and 172 are characterized by conspicuous high-frequency flow fluctuations with periods shorter than about 5 days. At 161 and 172, these fluctuations are strongly polarized along interisland channels. The situation at the other current meters is more complex, and simple visual inspection is not adequate for deciding if such oscillations occur there because of the presence of other motions with different periods and comparable or larger kinetic energy.

Spectral analysis of major axis components of currents and winds is therefore used to formally identify the high-frequency signal observed from current and wind records. The coherence function between different instruments is also estimated. For these analyses the nearly 6-month-long time series were divided into eight subintervals of length 21.3 days. Each subinterval was then Hanning windowed. A 50% overlapping was used, cross-spectra were computed, and the results were averaged over the subintervals to obtain spectral estimates at 1, 2, . . . cycles per 21.3 days. The 95% significance level, such that coherences exceeding this level would be obtained only one time in 20, were the records truly uncorrelated, was then obtained from Koopmans (1974) for 21 degrees of freedom (twice the number of subintervals divided by the factor 0.75 appropriate to the bandwidth of estimates made using the Hanning window). The bandwidth associated with these spectral estimates is about 0.125 cpd (8 days), whereas the high-

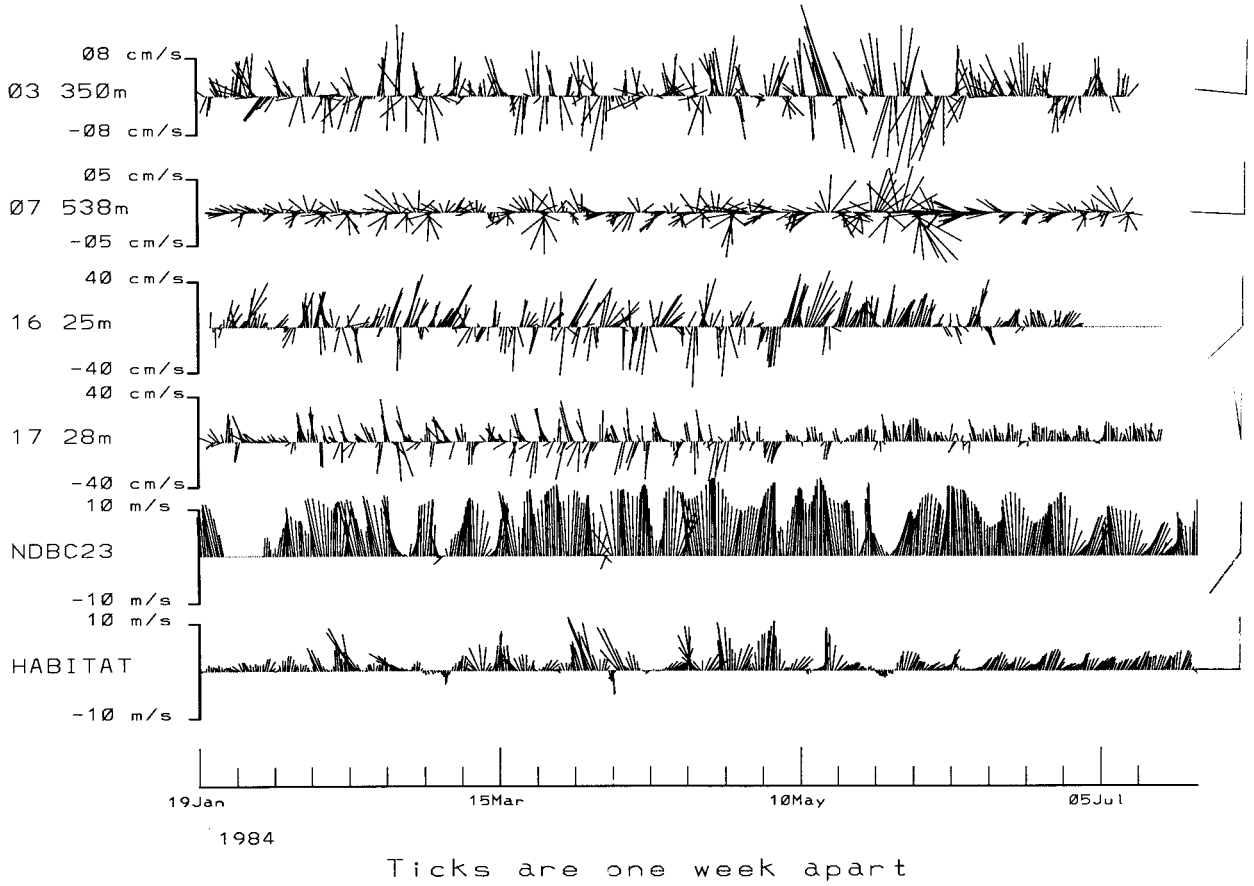

FIG. 2. Selected vector time series of currents at moorings 03, 07, 16, 17, and winds at mooring NDBC23 and platform Habitat. The wind and current velocities were low passed with a 38-h low-pass filter. The two arrows on the right of each series denote the major axis direction (vertical arrow) and the north direction.

frequency spectral peaks in Fig. 3 are centered at 8/21.3 cpd and are between 2/21.3 cpd and 4/21.3 cpd in width. The spectral estimates of Fig. 3 are thus averaged over about the width of the high-frequency peaks; correspondingly their width may be dominated by the averaging.

The major-axis variances partitioned by frequency for instruments 033, 161, and 172 as well as the squared coherence between major-axis currents for the three pairs of these are shown in Figs. 3a–c. These three pairs have the highest coherences among all possible combinations of current meters. All three individual records have in common a peak in the variance curve (an absolute maximum for instruments 161 and 172) and a highly significant maximum squared coherence of 0.60 to 0.70 in the 2.5–3.0-day band (the 95% confidence level is 0.26). The pair 033–073 (not plotted) also shows a significant maxima of squared coherence, 0.45, in the 2.5–3.0-day band. In the 4.5–5.2-day band, the currents at the two pass instruments are highly coherent among them (squared coherence is 0.6), but neither of them is coherent with the deep currents observed at the northern half of the western mouth or at the center of the channel. The phase functions (not shown) associated with the coherence shown in all panels of Fig. 3 showed an organized (almost linear) dependence with frequency. This supports the result obtained from the confidence levels in that the the corresponding coherences were unlikely obtained by chance.

Similar results for the wind stress at Hondo and MB22 and currents at instruments 033, 161, and 172 are shown in Figs. 3d–f. The variance of the wind stress at both Hondo and MB22 shows secondary peaks in the 2.5–3.0-day band while the squared coherence between winds and currents, significant in all three cases shown, reaches maximum values of 0.51 to 0.60 depending on the pair chosen. In contrast, the squared coherences calculated between these wind stations (or any others) and other 30-m current meters (e.g., 021, 031, 071) were not significant in the 2.5–3.0-day band. Coherences between instruments separated vertically on the same mooring were also low, with the exception of the pair 032–033, which has a maximum squared coherence of 0.40 in the 2.5–3.0-day band. In the 4.5–5.2-day band

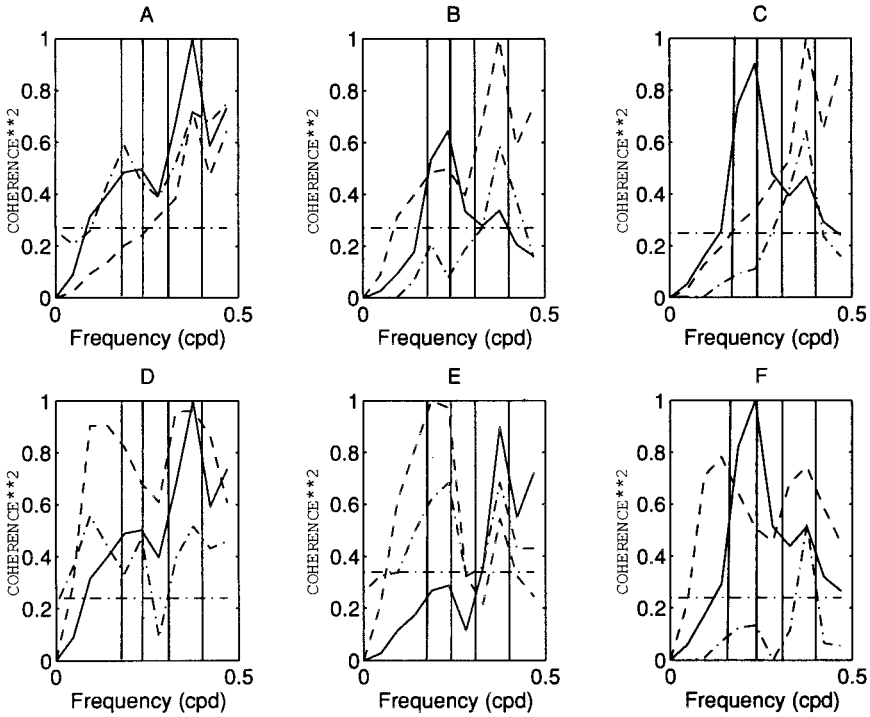

FIG. 3. Major axis variances (power spectrum multiplied by frequency) and squared coherences for selected pairs of currents at instruments 033, 161, and 172 and wind stress at stations Hondo and MB22. The squared coherence is plotted as a dot–dashed curve; the dot–dashed horizontal line represents the 95% confidence level. The vertical solid lines highlight the 2.5–3.0-day band and the 4.5–5.2-day band. Each variance curve of a pair was normalized by the maximum value of the pair while the horizontal axis is on a linear scale. In some plots an additional multiplicative scaling was applied to one of the curves for clarity in plotting. The pair and scaling for each panel are: (A) instruments 161 (solid)–172 (dashed), (B) instruments 033 $\times$ 5 (solid)–161 (dashed), (C) instruments 033 $\times$ 5 (solid)–172 (dashed), (D) instrument 161 $\times$ 3 (solid)–wind station Hondo (dashed), (E) instrument 172 $\times$ 3 (solid)–meteorological buoy MB22 (dashed), and (F) instrument 033 $\times$ 20 (solid)–wind station Hondo (dashed).

the currents at the interisland passes (161 and 172) are significantly coherent with winds at platform Hondo and MB22. Deep currents at mooring 03 were not significantly coherent with the local winds. Later, however, we will see that a coherent pattern of 4.5–5.2-day band currents with strong participation coming from these deep instruments is well coherent with modal wind time series. This significant coherence will emerge as a result of the filtering techniques to be described and applied in section 3.

In summary, these coherences suggest meteorological forcing of high-frequency (2.5–3.0- and 4.5–5.2-day band) currents at the interisland passes. They also would suggest some sort of connection between currents at the interisland passes and deep currents at the center of the channel and at the northern part of the western mouth in the 2.5–3.0-day band. Phases obtained from the cross-spectral analysis between pass currents and deep currents in this band show the latter lagging the former by a few hours (not shown) and an almost linear behavior in frequency for the few harmonics located inside the 2–4-day band. There was no evidence for direct communication between 1) high-frequency surface currents and deep currents immediately below and 2) high-frequency winds at the surface and near-surface currents away from the southern shelf. In the next section, and by analyzing the spatial structure of the dominant empirical function of the currents and its time correlations to local winds, we will test the ideas that the deep current oscillations are (i) uncoupled from near-surface current oscillations (if any) directly overhead in the water column, (ii) coupled to current oscillations in the southern shelf of the channel, and (iii) being, in some way, generated by local winds.

3. The wind-induced circulation

a. Near-surface (30 m) currents

1) INTRODUCTION

The foregoing section has documented that 2–4-day band winds in the SBC are well correlated with 2–4-day band currents in the inter-Channel Island passes and near the coasts as well as with currents at near-bottom

instrument 033 (on the northern slope of the western mouth). It is important to note also that the currents higher in the water column above these near-bottom instruments are among the most poorly correlated with the wind. A similar picture was found in the 4–6-day band where high-frequency motions are observed both at the passes and at the deeper instruments on moorings 03 and 07. However, the computed coherences did not reveal significant relationships between the deep currents and the winds and between the deep and the pass currents. The local winds were, in the 4–6-day band, well coherent with pass currents.

We attempt to examine the spatial structure of these components of the flow by constructing the empirical orthogonal functions (EOFs) in the 2–4- and in the 4–6-day bands for the entire array using the technique described in Wallace and Dickinson (1972). We do not compute one EOF in the 2–6-day band to, first, avoid the broadband effects pointed out by Merrifield and Guza (1990) and, second, because we want to study these two significantly different spectral peaks in winds and currents (Fig. 3) separately. For the currents, we use 50 scalar time series, 25 from the north components and 25 from the east components, that were each of them taken to complex series. The Hilbert transform of the real part defines the imaginary part of the complex time series. For narrowband signals it has the property of being 90° out of phase with respect to the real part. Defining the time series in this way will provide us with the vital phase information needed to describe the path of a given mode throughout the mooring array.

Fourier series were used to obtain the bandpassed data. In order to verify the performance of this filter, we estimated the amplitude and phase of the transfer function and the coherence between a given time series and its bandpassed version. In all selected cases and for both frequency bands (i.e., 2–4-day and 4–6-day bands), the amplitude of the transfer functions were between 0.96 and 1.03, the phase of the transfer functions between −4° and 5°, and the coherence function was always higher than 0.97.

From 100 Monte Carlo simulations a 99% confidence level was obtained for each mode described in this article. In all cases the 99% level was well below the estimated variance of these modes, for example, for the first current mode in the 2.0–4.0-day band the explained variance is 55% being the 99% level of 18.5%.

2) THE 2.0–4.0-DAY BAND

In the 2–4-day band, the first mode captures 55% of the variance in the band. It is highly correlated (0.8) with the first EOF mode of the winds, which captures 73% of the variance in the band. Since the amplitude time series of both (currents and winds) EOFs are complex, the correlation coefficient was computed between their real parts, which represent the time behavior of their modal wind speed. The EOF of the winds is also computed in the 2–4-day band and includes data from 5 stations (10 scalar time series). Figure 4 shows the cross-spectral analysis between the first wind mode and the first current mode. The squared coherence function shows that more than half of the variance of the currents can be predicted from the winds for the most energetic current band (i.e., 2.4–2.9-day band). In Fig. 4c it is seen that dominant modal winds lead dominant modal currents by about 0.75 day.

Figure 5 shows the spatial structure of the first mode of currents and winds. Co- and quadrature vectors are shown in Fig. 5 (top and bottom) respectively for 30-m currents and winds. Table 2 completes the description. The co- and quadrature vectors are obtained from the real and imaginary parts, respectively, of the first complex eigenvector. In each panel the modal winds lead the modal currents by 0.75 day. From Fig. 5 the sequence is as follows: In the top panel we first note maximum winds at NDBC23 and smaller winds inside the channel. Three quarters of a day later (still top panel) and at 30 m, water enters the channel at the eastern end and at the southern part of the western mouth. Anywhere else at 30 m and at the bottom instruments (not shown) of moorings 03 and 04 water leaves the channel. The recirculating pattern observed at the western end is discussed in A96. A quarter of a period later (about 0.75 day, bottom panel), winds are now maximum on the northern shelf of the channel and small at buoy NDBC23. Three-quarters of a day after these winds (bottom panel, winds) and three-quarters of a day after the currents shown in the top panel, water leaves the channel everywhere but at the northern part of the western entrance (top to bottom). Maximum water velocities occur at the interisland passes between the Santa Cruz and Santa Rosa Islands (161) and between the San Miguel and Santa Rosa Islands (172). The strong participation of buoy NDBC23 in the mode is evident from the top panel. The behavior of each velocity vector can be visually reconstructed from the co- and quadrature vectors: when the co- and quadrature vectors of a given instrument are at about 90° the behavior is rotary (e.g., 073), if they are colinear they are linearly polarized (e.g., 033). In both panels the east components of the 30-m flow at the northern and southern parts of the western entrance (i.e., moorings 02 and 05) have different signs as noted by several authors (e.g., Brink and Muench 1986) and in A96.

The EOF code is used to compute the variance contribution of each mode to each instrument. The least amount of variance explained by the first mode is for instrument 122 where it explains 43% of its total variance. At this location, the second mode is the second most important contributor explaining 14% of the total variance. This shows that the wind-induced currents have significant amplitude not only on the southern shelf but also at the eastern and western ends and in the deeper parts of the SBC. Figure 5 describes then, the dominant wind pattern and its induced currents. These currents

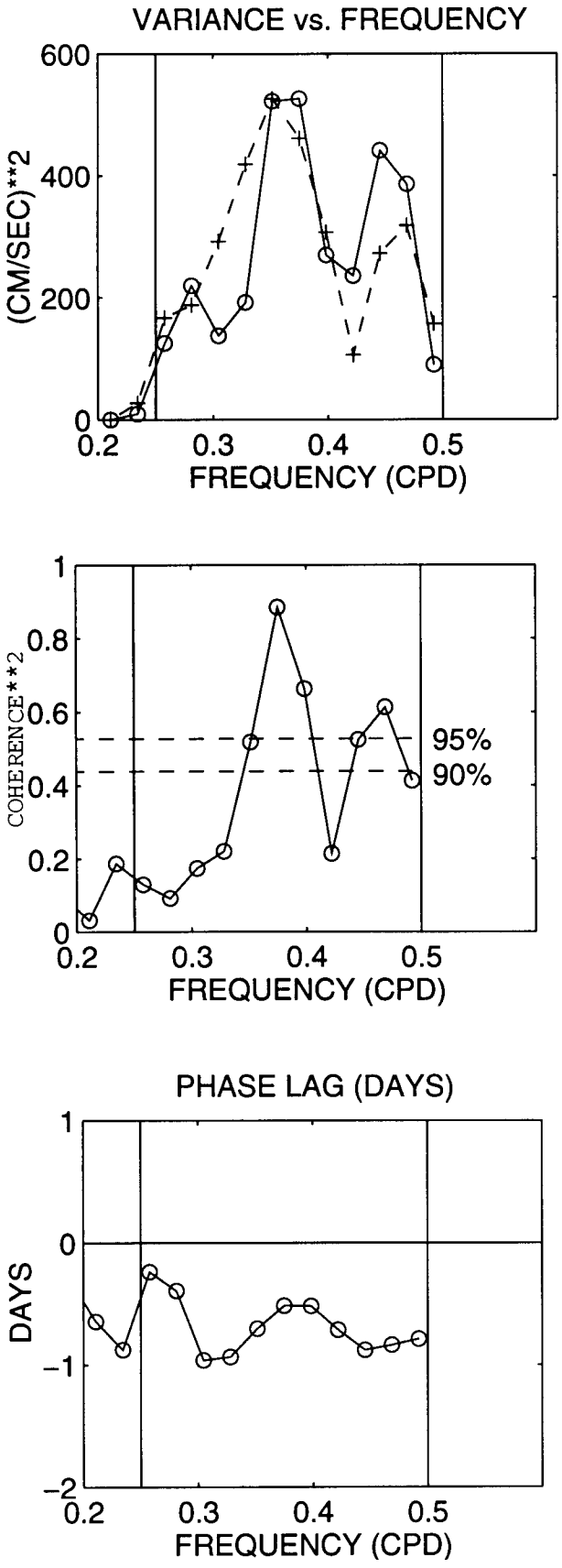

constitute the dominant spatially coherent channel-mode in the 2–4-day band.

The current vector time series were reconstructed using only the first EOF mode for each vector (a total of 25 vectors). Then the time lags corresponding to the maximum vector correlation among all instruments were estimated by computing the maximum (lagged) vector correlations, a method described in Mooers (1973). The results (Fig. 5 and Table 2) show 30-m currents at the center of the western mouth (deepest part) leading all other currents in the SBC. In general, the currents in the western end of the SBC lead currents eastward and southward of them. This sense of propagation agrees in general with the findings of Brink and Muench (1986); using 1983 current data they computed a time domain EOF at each mooring and then estimated the maximum vector correlations among the dominant modes from each of those moorings.

Table 2 gives a compact description of the spatial structure of the first EOF mode of the currents in the 2–4-day band. The wind-induced mode is characterized by a strong polarization at almost every location, as is evident from the larger variance concentrated along the major axis in comparison to the minor axis variance. From the major axis column and from the two columns on the right, we observe bottom intensification at the three deeper moorings of our array (namely, 03, 04, and 07). This topic is treated in detail in the next subsection. All other moorings show surface intensification and are located on waters shallower than 180 m with the exception of mooring 11 (also showing surface intensification), which is on a 300-m-deep bottom. Note that 30-m currents at all moorings located on the southern part of the channel (i.e., 05, 20, 16, 17, and 12, which are not sheltered by islands like 21) have their major axes oriented almost normal to the isobath (see column ''Dir'' in Table 2) and are anchored in waters shallower than 100 m. The remaining moorings show flows with major axis oriented about parallel to the local isobaths. Note that the three instruments (033, 161, and 172) having the larger values in the second column from the right, a measure of the signal-to-noise ratio, are those for which we found (section 2b) the maximum coherences among all possible combinations of instruments.

Figure 6 shows the temporal amplitude and phase corresponding to the first two modes of the currents and winds. There is a decrease in the amplitude of winds and currents after about day 100, which corresponds to

←

FIG. 4. Cross-spectral analysis between the first frequency domain EOF mode of the currents (55%) and the first EOF mode of the winds (73%) in the 2–4-day band. The two vertical lines in each panel mark the 2 and 4 day periods in which the EOF was computed. (a) Variance vs frequency. The wind variance (dashed line) is normalized against the maximum value of the current variances. (b) Squared coherence vs frequency. The horizontal line is the 95% confidence level. (c) Time lag (in days) vs frequency.

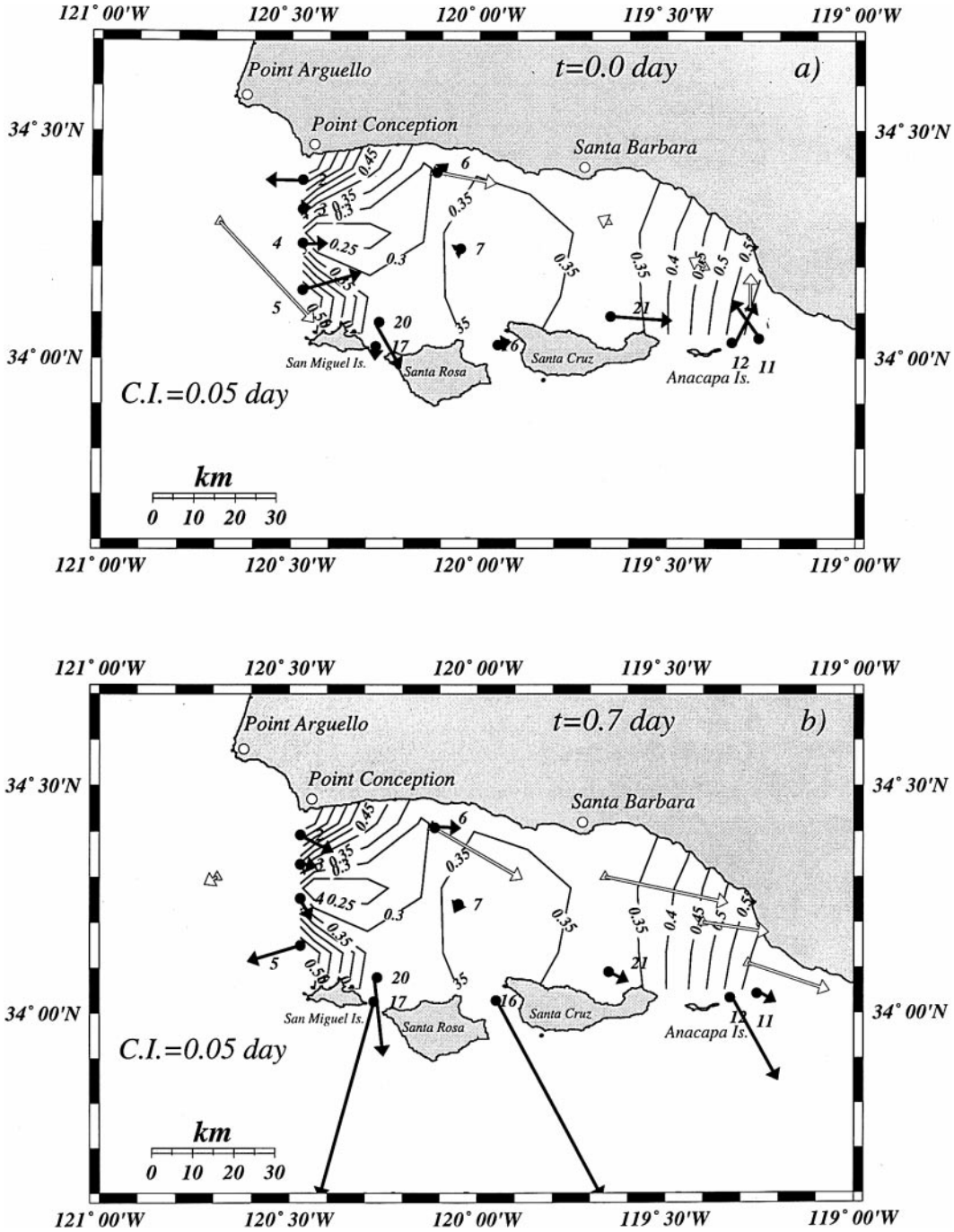

FIG. 5. Spatial structure of the first EOF modes of currents (black vectors) and winds (white vectors) in the 2–4-day band. Only the vectors at 30 m are shown. A complete description of this mode spatial structure is given in Table 2. Time lag (in days) contours (contour interval of 0.05 day) obtained from the maximum vector correlations of the 30-m currents reconstructed from the first EOF mode (same contours in both panels). These contours are shown along with (a) covectors (or real part of eigenvectors) of 30-m currents (black vectors and mooring locations marked by dots) and winds (white vectors and station location noted by triangles). (b) As in (a) but for quadrature vectors (or imaginary part of eigenvectors)

TABLE 2. Spatial structure of the first current frequency domain (2–4-day band) EOF mode. The time series at each instrument location were reconstructed using the first EOF mode. The Relief columns include both the total bottom depth, in meters, and the estimated isobath orientation, in degrees, relative to the east direction. Column Time lags (in days) shows the time delays with respect to instrument 041, which is leading all the other instruments in our array. The time lags corresponding to instruments located at 30 m are contoured in Fig. 5. Columns Maj and Min list the major and minor axis variance (in $cm^2\ s^{-2}$) at each instrument; Dir is the direction of the major axis relative to the east direction. Var1/varbp is the ratio of total modal variance, that is, var1 (major axis variance plus minor axis variance) to the total variance in the 2.0–4.0-day band, that is, varbp. Varbp/vartot is the ratio of the total variance in the 2.0–4.0-day band to the total variance in the original time series (low-pass filtered data, Fig. 2).

Instrument		Relief		Time lags	Principal axes			Var1/ varbp	Varbp/ vartot
ID	Depth (m)	H	O	(days)	Maj	Min	Dir	(%)	(%)
021	30	150	−16	0.75	5.20	0.30	−15	19	7
022	100			0.25	0.60	<0.01	12	4	10
031	30	366	−6	0.12	0.90	<0.01	−7	3	6
032	200			0.37	3.30	<0.01	−21	35	15
033	350			0.62	6.90	0.20	−23	69	29
041	30	476	−15	0.00*	2.10	0.10	−10	10	9
042	100			0.12	3.10	<0.01	−19	22	12
043	250			0.50	3.20	<0.01	−9	50	14
051	30	90	−11	0.75	13.00	0.70	28	58	9
052	65			0.62	7.40	1.00	34	67	16
061	30	150	−3	0.25	1.55	0.31	−4	14	7
062	100			0.12	0.43	0.02	2	3	10
071	30	563	−3	0.50	0.30	<0.01	45	2	7
073	538			0.50	0.50	0.11	−4	38	16
111	30	300	32	0.75	3.80	0.20	−47	27	9
112	80			0.50	0.30	0.20	22	9	6
113	150			0.75	0.65	<0.01	−49	13	9
121	30	98	−140	0.50	20.00	2.70	−68	43	22
122	80			0.62	5.20	0.30	−60	39	8
161	25	44	−65	0.37	127.00	0.25	62	92	38
172	28	33	−122	0.25	93.00	<0.01	75	98	75
201	30	73	180	0.25	13.30	2.50	85	65	16
202	65			1.00	8.60	0.40	7	62	29
211	30	183	−7	0.25	7.91	0.70	−7	28	17
212	80			0.12	1.82	0.40	20	16	17

* Reference.

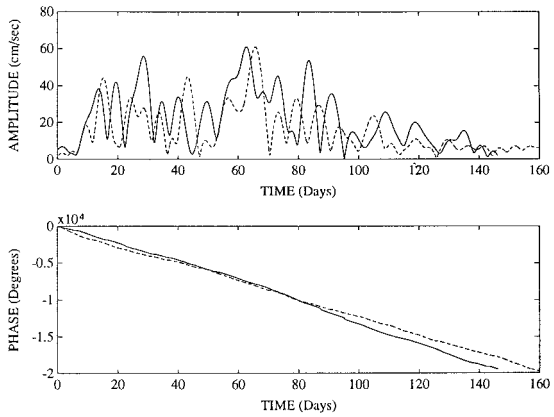

FIG. 6. Temporal eigenfunctions of currents (solid) and winds (dashed) corresponding to the first frequency domain (2–4-day band) EOF modes of the current and wind fields respectively. Day 0 corresponds to 31 January 1984. (a) Amplitude time series. The wind time series is normalized against the maximum value of the currents time series. The maximum wind speed is 13.2 m s^{-1}. (b) Phase time series. For the sake of comparison the phase at time zero of both curves was set to zero.

10 May, a fact also noticed by Brink and Muench (1986) from low-pass filtered data. The phase versus time function shows an approximately linear behavior for currents and winds. An ''average frequency'' (the frequency of a single sinusoidal wave that would be needed to give the same change of phase in the same amount of time) can be estimated from these curves. This gives periods of 2.75 and 2.85 day for currents and winds respectively. The amplitude time series of the modal currents was contrasted with the amplitude time series of the transports (A96) band passed in the 2–4-day band. Figure 7 shows this comparison between modal currents and bandpassed transports estimated at the interisland passes, at the western mouth and at the eastern mouth of the SBC. It is seen that the variance in this band, mostly wind-induced, fluctuates along with the net mass transport passing through the SBC. Thus, Fig. 7a shows that the first EOF of the currents passing through the interisland passes is almost entirely dominated by the mass transport. This result was confirmed, for the common portion of the record, when we computed an additional

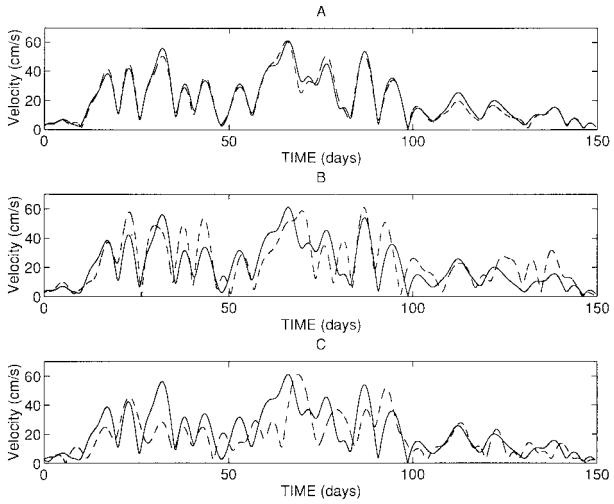

FIG. 7. Temporal amplitude of the first EOF mode, solid lines (same mode shown in Fig. 6), compared against the time series of the transport passing through (a) the interisland passes, (b) the western mouth, and (c) the eastern mouth. All transport series were bandpassed in the 2–4-day band and were normalized against the maximum value of the modal time series. Day 0 corresponds to 24 January 1984.

set of EOFs adding data from two more current meters (having shorter records). They were located on mooring 16 (at 38 m) and the other one on mooring 17 (at 25 m).

3) THE 4.0–6.0-DAY BAND

A situation similar to that one described above in the 2–4-day band happens in the 4–6-day band. The first mode of the currents explains 47% of the total variance in the 4–6-day band, while the first mode of the wind field explains 64% of the total wind variance in the same band. The 30-m vectors for both calculations are shown in Figs. 8a,b. In both panels the wind field leads the corresponding currents by almost two days. At time zero (Fig. 8a) winds are westward to northwestward on the northern shelf of the channel and are very small at buoy NDBC23 (Point Conception). The 30-m currents on the northern half of the western entrance are westward, while on the southern half they are eastward. In fact, the maximum amplitudes take place on the northernmost and southernmost 30-m instruments of the western mouth (i.e., 021 and 051). A quarter of a period later (1.25 days), it is seen that eastward to southeastward winds imply, at time zero (Fig. 8b), that 30-m currents are out of the channel on the eastern and southern boundaries of it (i.e., on moorings 05, 17, 16, 12, and 11). At the northern part of the western mouth (moorings 02, 03, and 04) the flow at 30 m has an into-the-channel component. At times $t = \pi$ and $t = 3\pi/2$, currents and winds will have the same amplitude but opposite directions to those at $t = 0$ and at $t = \pi/2$ respectively. As in Fig. 5 (2–4-day band), the time lag contours of Fig. 8 (4–6-day band) show also that 30-m currents at the center of the western mouth lead all other currents in the channel (see also Table 3), moving from west to east with some important distortions (i.e., the propagation is not monotonic from west to east) due to the effect of the pass currents (also, as in the 2–4-day band). The northern and southern ends of the western mouth (moorings 02 and 05, respectively) also, as in the 2–4-day band, feel the arrival of the signal much later than instruments located in the channel interior (note the slow northward and southward propagation from instrument 03).

Figure 9 shows the amplitude and phase time series of the first frequency domain, in the 4–6-day band, EOF modes of the current and wind fields. As in Fig. 6 (2–4-day band), the similarity between both time series is clear, implying that the flow structure shown in both panels of Fig. 8 is basically wind driven by the modal wind field shown in the same figure. This visual correlation is quantified through a cross-spectral analysis between modal wind and currents (Fig. 10). The dominant wind pattern leads the dominant current pattern by about 1.5 day (both shown in Fig. 8). All three harmonics lying in the 4–6-day band (5.3, 4.7, and 4.2 days) are highly coherent.

We can attach physical meaning to the first frequency domain EOF mode by comparing the first-mode amplitude time series to the amplitude of the transport time series estimated at the eastern, western, and southern boundary, so the SBC (Fig. 11). Thus, currents shown in Fig. 8 represent the circulation implied by the mass transport entering the channel through its western mouth in the 4–6-day band. This can be seen from the distribution of 30-m time lags (Fig. 8). These lags were estimated as described above for the 2–4-day band. It can be seen, as it happened in the 2–4-day band, that the 30-m currents at the center of the western mouth lead all other currents in the channel in the 4–6-day band.

Table 3 shows a summary of the 4–6-day band first-mode spatial structure for all instruments. At moorings 03 and 04 we observe bottom-trapped amplitudes that will be analyzed in the next subsection. By comparing the signal-to-noise ratio (column varl/varbp) between the 2–4-day band (Table 2) and that in this table at instrument 033, it can be explained why we were not able (in section 2b) to find significant coherences between currents at instrument 033 and both currents at the passes and winds. In the 2–4-day band the signal at instrument 033 (Table 2) is dominant (69% of the total band variance), while in the 4–6-day band the signal at 033 (Table 3) is not (23% of the total band variance). However, the EOF analysis, which further increases the signal-to-noise ratio, shows that there is a significant part of the flow at 033 that is both coherent with currents at the passes and with the local wind field in the 4–6-day band.

b. Near-bottom currents

The velocity time series at current meter 033 (Fig. 2) suggests organized motions at 350 m (25 m above the

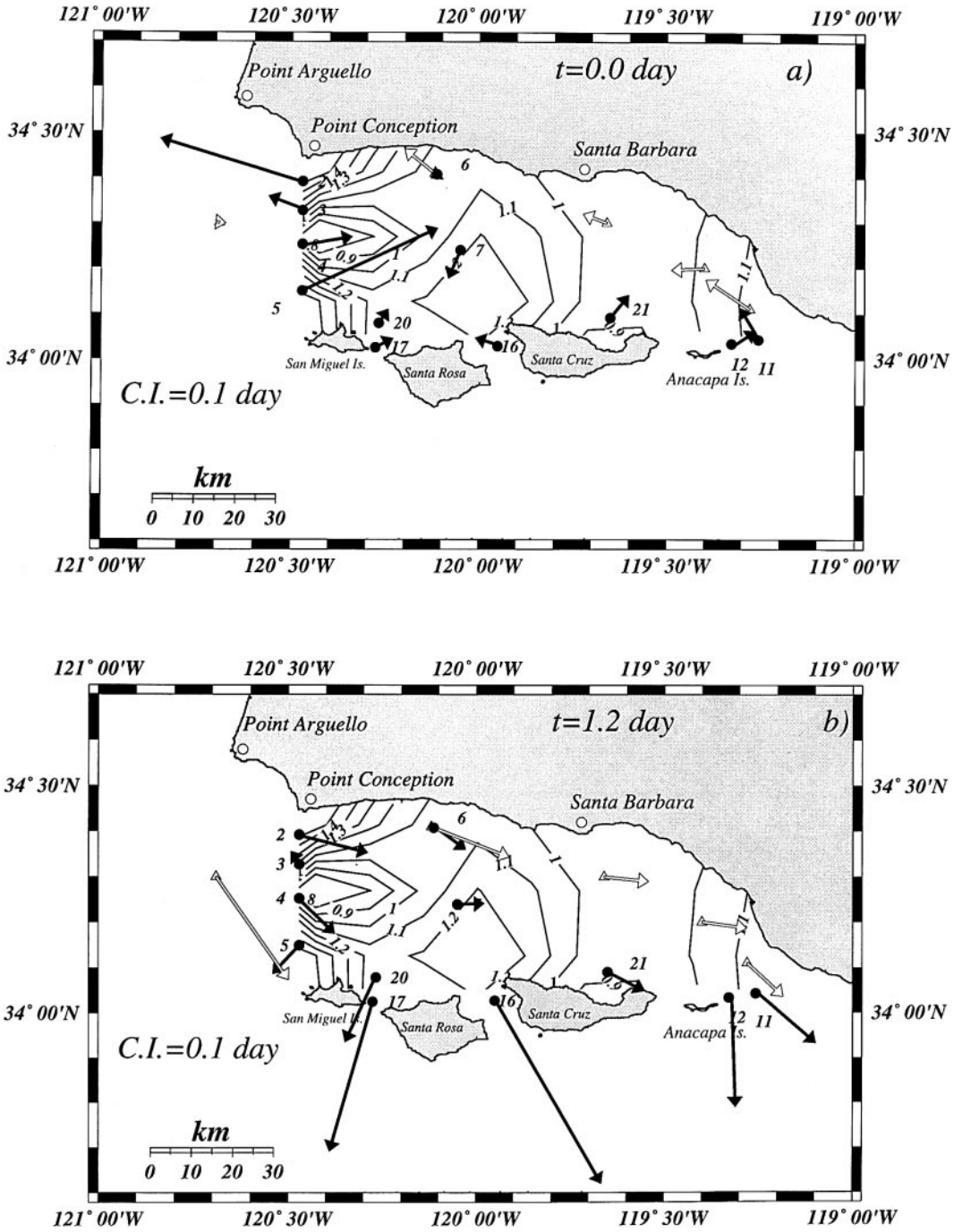

FIG. 8. Spatial structure of the first EOF modes of currents (black vectors) and winds (white vectors) in the 4–6-day band. Only vectors at the 30-m level are shown. A complete description of this mode spatial structure is given in Table 3. Time lag (in days) contours (contour interval of 0.1 day) obtained from the maximum vector correlations of the 30-m currents reconstructed from the first EOF mode (same contours in both panels). These contours are shown along with (a) covectors (or real part of eigenvectors) of 30-m currents (black vectors and mooring locations marked by dots) and winds (white vectors and station location noted by triangles). (b) As in (a) but for quadrature vectors (or imaginary part of eigenvectors)

TABLE 3. Spatial structure of the first current frequency domain (4–6-day band) EOF mode. The time series at each instrument location were reconstructed using the first EOF mode. The Relief columns include both the total bottom depth in meters and the estimated isobath orientation in degrees relative to east. Column Time lags (in days) shows the time delays with respect to instrument 031 (*), which is leading all the other instruments in our array. The time lags corresponding to instruments located at 30 m are contoured in Fig. 8. Columns Maj and Min list the major and minor axis variance (in $cm^2\ s^{-2}$) at each instrument; Dir is the direction of the major axis relative to the east direction. Var1/varbp is the ratio of total modal variance, that is, var1 (major axis variance plus minor axis variance) to the total variance in the 4.0–6.0-day band, that is, varbp. Varbp/vartot is the ratio of the total variance in the 4.0–6.0-day band to the total variance in the original time series (low-pass filtered data, Fig. 2.)

Instrument		Relief		Time lags	Principal axes			Var1/ varbp	Varbp/ vartot
ID	Depth	H	O	(days)	Maj	Min	Dir	%	%
021	30	150	−16	1.80	23.7	0.02	−17	46	12
022	100			1.12	2.3	0.16	−4	10	19
031	30	366	−6	0.00*	1.3	0.05	−25	5	8
032	200			1.46	1.5	<0.01	0	15	22
033	350			0.70	3.3	<0.01	−32	23	43
041	30	476	−15	0.33	3.4	0.90	−16	13	15
042	100			1.00	3.0	0.75	−31	20	19
043	250			1.00	3.8	0.14	−5	61	18
051	30	90	−11	1.96	20.6	0.18	27	69	15
052	65			1.65	3.6	0.11	25	43	12
061	30	150	−3	1.00	1.3	0.07	−35	13	6
062	100			1.72	0.2	0.01	−5	2	5
071	30	563	−3	1.65	1.1	0.41	42	5	11
073	538			0.77	0.4	0.10	43	15	54
111	30	300	32	1.23	6.7	0.08	−44	62	6
112	80			1.00	2.8	0.02	−42	46	7
113	150			0.65	1.0	<0.01	−46	14	11
121	30	98	−140	1.00	10.4	0.41	−89	45	9
122	80			1.00	5.3	0.26	−71	65	6
161	25	44	−65	1.00	55.8	0.22	−59	90	13
172	28	33	−122	1.00	21.6	0.18	74	91	10
201	30	73	180	1.19	4.3	0.01	65	37	7
202	65			1.60	1.8	0.12	5	29	4
211	30	183	−7	0.77	1.5	0.70	−19	11	10
212	80			0.52	4.2	0.03	3	30	16

* Reference.

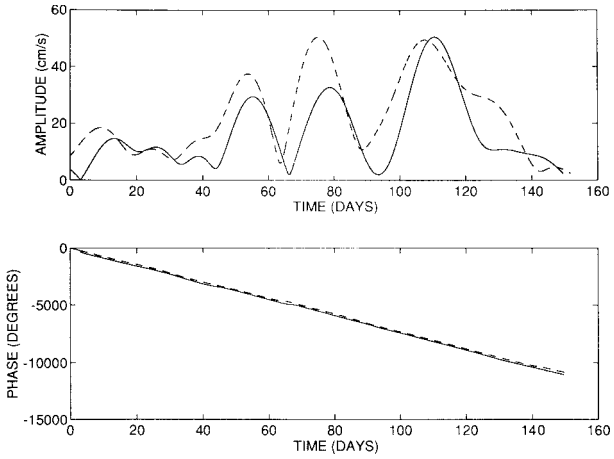

FIG. 9. Temporal eigenfunctions of currents (solid) and winds (dashed) corresponding to the first frequency domain (4–6-day band) EOF modes of the current and wind fields. Day 0 corresponds to 31 January 1984. (a) Amplitude time series. The wind time series is normalized against the maximum value of the currents time series. The maximum wind speed is 7.1 m s^{-1}. (b) Phase time series. For the sake of comparison the phase at time zero of both curves was set to zero.

bottom) that seem to disappear or to be masked by other motions higher up in the water column. Gunn et al. (1987) speculated that these deep oscillations could be explained in terms of Rhines' (1970) theory of bottom-trapped waves. In this section, we compare the picture obtained from the EOF of the currents of the previous section (e.g., Table 2) with the predictions of that theory. We expect the comparison to be good only in the deep water away from regions (e.g., the interisland passes) where the local geometry invalidates some of the assumptions of the theory.

Basically, bottom-trapping takes place in a stratified and rotating fluid over a sloping bottom when the horizontal scale of the flow is smaller than the deformation radius $R_d = NH/f$, where N is the buoyancy frequency, H is the local depth, and f is the local Coriolis parameter. Bottom-trapped waves are characterized by a balance between relative vorticity and the local change of vortex stretching, that is,

$$\nabla^2 p_t + \frac{f^2}{N^2} p_{zzt} = 0, \tag{1}$$

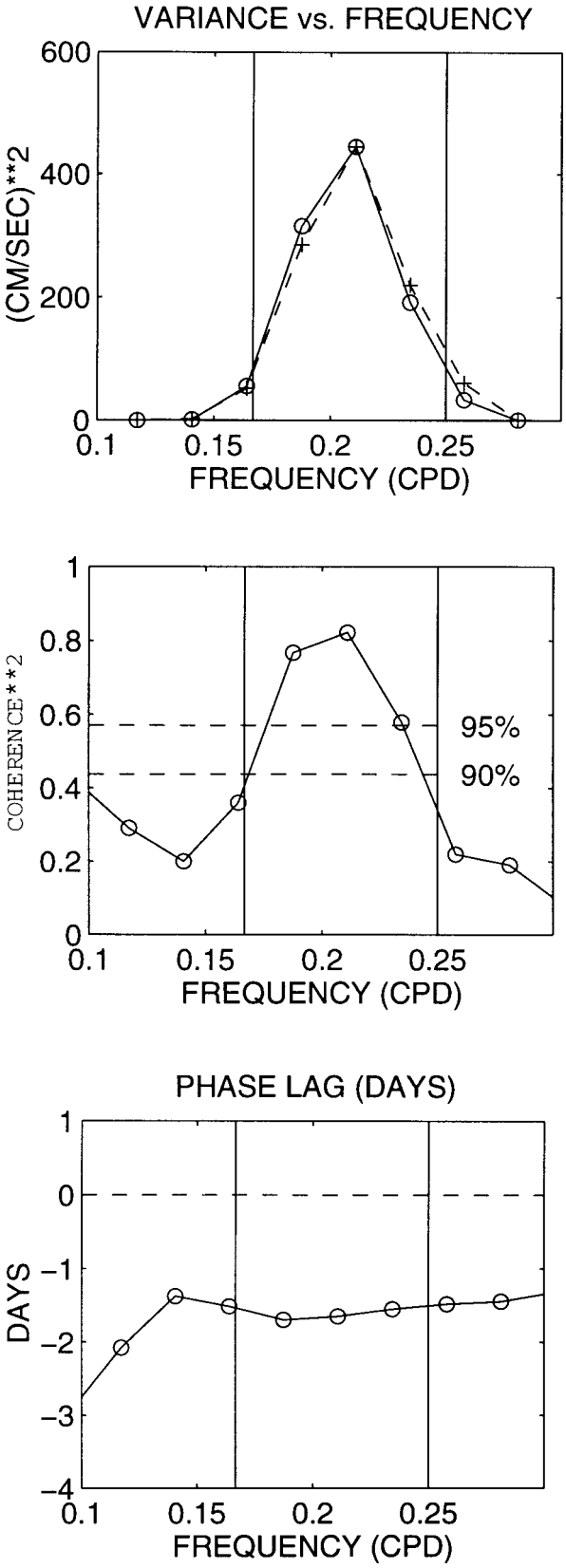

and owe their existence to the earth's rotation, to stratification, and to the tilting of the oceanic bottom. Here p is pressure and subscripts denote partial derivatives with respect to time (t) and the vertical coordinate (z). The horizontal velocity field associated with a plane bottom-trapped fast baroclinic wave over a uniformly sloping bottom is (Rhines 1970)

$$[u(x, y, z, t), v(x, y, z, t)] = U_0 \cosh\left(\frac{z}{\delta}\right) \exp[i(kz + ly - \sigma t)][-l, k], \quad (2)$$

with dispersion relation

$$\sigma = -\frac{N}{K}(kb_y - lb_x). \quad (3)$$

Here σ and K are the wave frequency and the modulus of the wavenumber vector (which has components k and l in the zonal and meridional directions respectively). The components of the topographic gradient ∇b are b_x and b_y in the zonal and meridional directions respectively, u and v are the zonal and meridional horizontal velocity components, U_0 is the flow speed at the bottom, and the scale δ of vertical decay is given by

$$\delta = \frac{fL}{N}, \quad (4)$$

where L is the horizontal scale equal to K^{-1}.

We attempt to compare this plane wave solution with our observations as follows. We think of the plane wave solution as a local description, valid over the more or less uniformly sloping northern shelf of the SBC, of the SBC-wide high-frequency flow system described from the observations in section 3a. We take $f = 8.2 \times 10^{-5}$ rad s^{-1}, adopt a constant value $N = 4 \times 10^{-3}$ rad s^{-1} (Gunn et al. 1987) for the Väisälä frequency, idealize the northern shelf as having slope $b_x = 0$, $b_y = 2 \times 10^{-2}$ (Gunn et al. 1987), and set the wave frequency equal to the frequency at which the variances at pass instruments 161 and 172 and deep northern slope instrument are maximum in the 2–4- and 4–6-day-bands; $\sigma = 2.64 \times 10^{-5}$ rad s^{-1} and $\sigma = 1.48 \times 10^{-5}$ rad s^{-1} respectively.

From the vertical decay of wave amplitude (Table 1) between deep instrument 033 and intermediate depth instrument 032, we estimate the vertical decay scale δ appearing in (2) to be about 300 and 280 m in the 2–

←

FIG. 10. Cross-spectral analysis between the first frequency domain EOF mode of the currents (47%) and the first frequency domain EOF mode of the winds (64%) (both EOFs were computed in the 4–6-day band). The real part of the first mode time series of winds and currents are used to compute the spectral functions. (a) Variance vs frequency. The wind variance (dashed line) is normalized against the maximum value of the current variance. (b) Squared coherence vs frequency. The horizontal line is the 95% confidence level. (c) Time lag (in days) vs frequency.

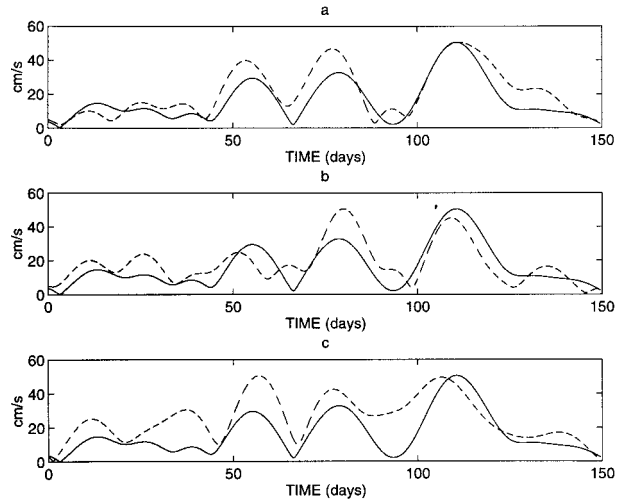

FIG. 11. Temporal amplitude of the first EOF mode (same as Fig. 9) compared against the time series of the transport passing through (a) the interisland passes, (b) the western mouth, and (c) the eastern mouth. All transport series were bandpassed in the 4–6-day band and were normalized against the maximum value of the modal time series. Day 0 corresponds to 24 January 1984.

4- and 4–6-day bands respectively. From (4) this fixes the size of the horizontal wavenumber K as $= 6.83 \times 10^{-2}$ rad km^{-1} in the 2–4-day band and K as $= 7.30 \times 10^{-2}$ rad km^{-1} in the 4–6-day band. In the 2–4-day band, the corresponding horizontal wavelength is about 92 km ($L = 14.6$ km) and the longshore phase speed is about 33 km day^{-1}. In the 4–6-day band these values are 86 km ($L = 13.7$ km) and 18 km day^{-1} respectively. Unfortunately, no other mooring was placed on the slope eastward of mooring 03 to allow us to make any phase speed or lag comparison against the ones predicted by the linear fit. Mooring 06 was placed on a bottom 150 m deep, too shallow to be able to detect the type of motions present at mooring 03. The dispersion relation (3) now fixes the direction of the horizontal wavenumber vector to within the choice of sign of the north–south component l of the wavenumber. But only one of the two choices will result in the observed polarization of the velocity vector.

With the choice of north–south wavenumber shown by the asterisk in Fig. 12, the wavenumber vector for the 2–4-day band is oriented about $-109°$ with respect to the generally east–west trending isobaths near mooring 03. In the 4–6-day band this angle is $-101°$. From (2) above, this implies that the velocity vector is oriented at 90° to the wavenumber vector, that is, along about $-19°$ and $-11°$ in the 2–4- and 4–6-day bands, both at the bottom and higher up in the water column. This prediction of the plane wave theory compares favorably with the observed polarization directions of $-23°$ (2–4-day band) and 0° (4–6-day band) at instrument 033 and $-21°$ (2–4 day band) and $-32°$ (4–6-day band) at instrument 032 relative to isobaths. Similar angles can be measured also from the low-passed vector time series shown in Fig. 2. Note that it corresponds to the propagation of wave energy toward shallower water.

We estimate the vertical decay scale from observations at mooring 03 rather than at neighboring moorings 02, 04, or 07 because mooring 03 is the only mooring (a) placed on a deep bottom, (b) placed on a steep slope, and (c) sampling flow both very near the bottom and somewhat farther up in the water column, yet not so near the surface that the variance would be dominated by local wind effects or by process(es) shown to exist in section 3a. The above estimate for the vertical scale δ is the same that is obtained if one takes the square root of the ratio between the variances of instruments 032 (variance not plotted in Fig. 3) and 033 in the narrow 2.6–2.8-day band where variance and coherence are maximum for both instruments. The estimated value of δ thus does not appear to depend sensitively on bandwidth.

The horizontal wavelengths (92 and 86 km) are too large for us to expect that a WKB modification of the plane bottom-trapped wave fit to the observations at moorings 03 and 04 will predict the flow at mooring 07 (center of the channel), yet it is worth noting that near-bottom flow there, although small, is nonetheless very well correlated with both SBC winds and the currents at the passes between the islands; moreover, the first EOF mode accounts for 38% of the bandpassed variance there.

Time lags between the 2–4-day band flow of the first EOF mode at the interislands passes (e.g., 161) and that at the deep central SBC mooring (073) and at the deep mooring over the northward sloping relief in the western mouth of the SBC (instrument 033) are, respectively, 0.12 and 0.25 day. These are about the phase differences that would be predicted for a bottom-trapped wave with the foregoing parameters f, N, and b_y between locations lying on an isobath and separated by the horizontal distances passes 07 and passes 03. The agreement could be in part fortuitous, since the actual stations do not lie along an isobath, and the phase differences are too small to be determined very reliably; yet it is worth noting that the observed phase differences are not grossly different from the order of magnitude suggested by the theory. In the 4–6-day band, events in the deep and passes currents happened almost simultaneously. However, these phase differences are too small to be determined very reliably.

The vertical decay scales of 300 and 280 m (from the 2–4- and 4–6-day bands respectively), estimated from data at mooring 03, are sufficiently small and moorings 03 and 04 are in sufficiently deep water that local application of Rhines' original theory, with its assumption of infinitely deep water above the sloping bottom, is reasonable at those moorings. Allowance for water depth shoaling to zero at a nearby coast is made in the numerically coastally trapped wave solutions of Brink and Chapman (1985), whose lowest mode over a uniformly deepening shelf reduces to Rhines' plane bot-

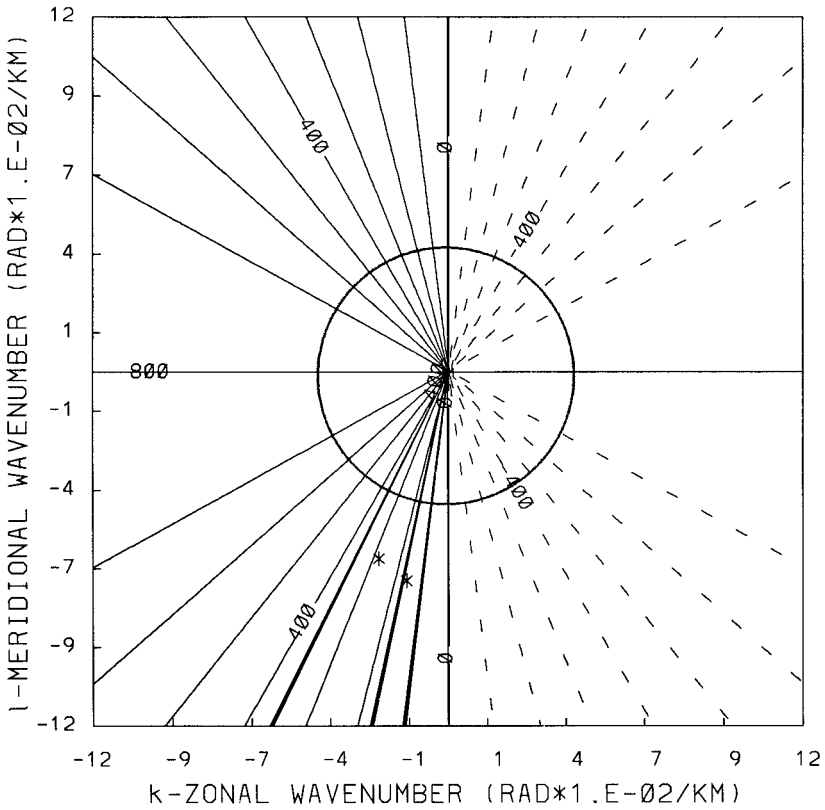

FIG. 12. Isolines of constant frequency σ (units of 0.137 cpd, i.e, period of 7.3 day) in the plane whose axes are the zonal and meridional wavenumber components k and l for the dispersion relation (3) with isobaths trending east–west and with a buoyancy frequency of 2.3 cph and a bottom slope of 0.02 upward toward the north. The circle corresponds to the Rossby radius and the asterisks denote the wavenumbers emerging from the plane wave fit (section 3) to observations at mooring 03 (the asterisk closer to the $k = 0$ axis corresponds to the wave found in the 4–6-day band, while the other one corresponds to the wave found in the 2–4-day band). The three heavy lines in the third quadrant bound the 2–4- and the 4–6-day bands. Inside the circle the dispersion relation is no longer valid.

tom-trapped wave in water deeper than the bottom trapping vertical scale. We computed the first mode of coastally trapped waves using the model of Brink and Chapman (1985). At mooring 02, 30 m below the surface (instrument 021), the isotachs (not shown) are about the same amplitude as bottom motions at mooring 03 (instrument 033) but 180° out of phase. We do not observe such a phase shift between the 2–4-day motions at moorings 03 and 02 in our first mode.

Note that 25% errors in the estimation of either the buoyancy frequency or the bottom slope will result in a range of polarization directions (for instance, for the 2–4-day band analysis) varying between 15° and 26°, values reasonably consistent with the observations shown in Fig. 5. A 25% error in the estimation of either the vertical scale of decay or the buoyancy frequency will result in horizontal wave scales varying between 11 and 18 km, both values still smaller than the deformation radius. Introducing these errors will still keep these motions in the parameter space corresponding to bottom-trapped baroclinic Rossby waves (Rhines 1977, p. 215).

We now check the values of parameters defining the range of validity of the linear theory. If the waves are to be bottom-trapped, then the horizontal scale must be small enough that the corresponding vertical scale as determined from (4) is substantially less than the total water depth. This forces the horizontal scale L to be substantially less than the internal deformation radius R_d. For our parameters R_d is about 24 km, substantially larger than the range of horizontal scales quoted immediately above. The estimated Rossby number Ro based on these horizontal scales is

$$\mathrm{Ro} = \frac{U_0}{fL} = 7 \times 10^{-2} \ll 1,$$

where U_0 (=8 cm s^{-1}) is the amplitude appearing in (2).

We finally compare these motions to those observed from a single mooring by Thompson and Luyten (1976)

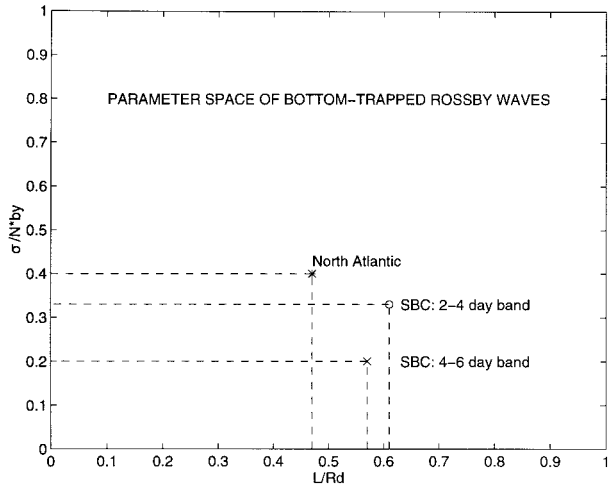

FIG. 13. Location, in the parameter space occupied by the theory of bottom-trapped topographic Rossby waves (Rhines 1970), of the present SBC observations in the 2–4- (o) and 4–6- (x) day bands (circle) and of the western North Atlantic observations (star) of Thompson and Luyten (1976). They observed bottom trapping in the 8–20-day band. The horizontal axis is the ratio of the wave horizontal scale (L) to the local Rossby radius $R_d = NH/f$. The vertical axis is the ratio of the wave frequency σ to the maximum possible bottom-trapped wave frequency $\sigma_c = Nb_y$. Note that the horizontal axis could also have been represented by δ/H since these waves satisfy $\delta/H = L/R_d$, where H is the local water depth and δ is the vertical scale of decay.

in the North Atlantic (see also Rhines 1977). For both cases, Fig. 13 plots the wave frequency σ and the wave horizontal scale L, in units of cutoff frequency, σ_c (maximum wave frequency for a given stratification and bottom slope), and Rossby radius respectively. Although the flows observed in the SBC in the 2–4-day band (and in the 4–6-day band) have very different horizontal and vertical scales and periods [14.6 km (13.7 km), 300 m (280 m), and 2.75 days (4.9 days) versus 20 km, 1200 m, and 15 days], they are very close to one another in the parameter space of Fig. 13, and so are in fact dynamically very similar.

4. Discussion

The observations, due to their low spatial resolution, throw little light on the mechanism(s) generating the deep flow oscillations, mainly observed at the northern slope of the western mouth and at the center of the channel. Brink (1989) points out that bottom-trapped motions are unlikely to be generated by direct wind forcing given the minimum amplitude attained by this type of motions at the surface.

Other possibilities, we speculate, are any processes that generate strong currents within the inter–Channel Islands passes and/or the southern shelf, barotropic or baroclinic, coherent with high-frequency SBC winds; once in the water that energy can then propagate into the deep water of the SBC as a field of bottom-trapped waves. A possible forcing mechanism of the deep currents could thus be the cross-isobath flow observed at 30 m at the open boundaries on the southern shelf, that is, at moorings 05, 20, 16, 17, and 12, but the 1984 data set is not spatially dense enough to map the spatial structure of the hypothesized bottom-trapped wave field. It has been suggested (J. Barth 1997, personal communication) that the origin of the cross-isobath flow that forces the topographic waves is from the wind-driven jet flowing down from the north off Point Conception and then impinging on the shelf off San Miguel Island. Again, the observations are not spatially dense enough to verify these hypotheses.

The implications for spatial structure can be discussed from several theoretical points of view. We first note that our plane wave estimate of horizontal wavelength suggests that, at the frequencies we observe, groups of bottom-trapped waves must be at least as large as the SBC in horizontal extent; ray tracing away from the hypothesized generation regions near the Channel Islands is not likely to provide a good quantitative description of the wave field.

From moored current meters in the Santa Monica Basin, Hickey (1992) found systematic propagation of phases across the basin at periods of order 17–35 days, substantially lower than the frequencies considered here. By (4) this implies vertical trapping scales as great as the water depth itself; that is, in accord with Hickey's observations, these low-frequency motions are not bottom-trapped. Both the Santa Monica Basin and the western SBC deep basin are of roughly similar lateral extent and water column stratification. We speculate that bottom-trapped waves such as the ones we have documented in the SBC are not excited in Santa Monica Basin because there are in there no localized regions that play the role of the shallow interislands passes and/or the southern shelf in efficiently transferring energy from winds to bottom-trapped waves.

In section 3b it was mentioned that the longshore velocity profile obtained from the coastally trapped wave (CTW) linear model of Brink and Chapman (1985) does not completely agree with the observations. The model predicts, for the first CTW mode, alongshore currents in opposite directions at the locations of instruments 021 and 033. This does not happen in the observed currents. There are three reasons why such a phase shift might not occur at mooring 02. The first is that the model solutions are for an infinite straight coast, yet mooring 02 is about 10 km off Point Conception, where the coast takes an abrupt turn northward. The second is that in the model's solution the phase shift is associated with the complete reflection, at the coast, of bottom-trapped energy coming up the sloping bottom from the deep sea. Failure to see the phase shift at mooring 03 may mean that this reflection is not occurring, either because the coast turns abruptly or because frictional effects become sufficiently important, as the contours

of Fig. 5 seem to suggest. The third possibility is that data recorded at mooring 03 are the coherent sum of such a phase-reversed bottom-trapped wave motion plus a directly wind-driven local response.

The only major discrepancy between the 2–4 and the 4–6 day is in the time lags of the deep instruments (i.e., 033, 043, and 073) relative to the passes. In the 2–4-day band currents at the passes lead deep currents at 073, 043, and 033 (in both the analyzes of sections 2b and 2a). In the 4–6-day band, events in the deep and passes currents happen almost simultaneously. However, it should be kept in mind that these phase differences are too small to be determined very reliably; yet it is worth noting that the observed phase differences are not grossly different from the order of magnitude suggested by the theory of bottom-trapped Rossby waves.

The variance peaks in both currents and winds are remarkably sharp. We might have invoked basin resonance to rationalize the sharpness of the current peak if we had found strong evidence of coastal or boundary reflection, but the foregoing discussion suggests that such reflection is not strong. The sharpness of the peak in current variance may simply reflect the sharpness of the peak in wind variance, for which we have no ready explanation.

5. Summary

From the spatial and temporal eigenfunctions of currents and winds and from available satellite images (not shown), the dominant current mode described above would represent a channel-wide response to upwelling events taking place north of Point Conception (northwestward of the SBC). The upwelling-related (equatorward) currents cause a net inflow of mass into the western end of the channel, which is compensated by an outflow passing through both the interisland passes and through the eastern mouth of the channel. As a result of the narrowness and shallowness of the passes in particular and of the shallowness of the southern shelf in general, high flow speeds are attained there that, we speculate, could force deep high-frequency motions both at the center of the SBC and at the northern half of its western mouth.

The current meter observations from the 1984 experiment reveal the existence of energetic high-frequency (period of about three days) currents both in the shallow passes between the Channel Islands (total depth about 40 m) as well as at the deepest instruments (25 m above the bottom in the center of the channel where the total depth is 563 m, 16 m above the bottom at the north slope of the western mouth of the channel where the total depth is 366 m). An important picture emerging from these observations is of deep high-frequency currents that, in general, 1) show an increase of their amplitude with depth (bottom trapping), only observable at the three deeper moorings (03, 04, and 07); 2) are not significantly correlated with currents directly overhead in the water column; 3) are highly lag correlated with high-frequency currents in the inter-Channel Islands passes; 4) show lags, from instrument to instrument, that are consonant with the Rhines (1970) bottom-trapped wave solutions; 5) are linearly polarized along a direction close to the trend of isobaths, again in consonance with the Rhines (1970) bottom-trapped wave solutions; 6) are significantly correlated with the same winds that are very highly correlated with high-frequency currents in the passes, and for the three deeper moorings mentioned in (1) the wind–current correlation increases with depth; (7) are dynamically similar to the bottom-trapped waves found in the North Atlantic by Thompson and Luyten (1976); and 8) are well inside the parameter space corresponding to bottom-trapped topographic Rossby waves (Rhines 1977), even when we introduce 25% errors in the estimation of those parameters.

Acknowledgments. Funding for this study was provided by the Minerals Management Service of the U.S. Department of the Interior under Cooperative Agreement 14-35-0001-30571. We especially thank Jack Barth, who as a reviewer shared with us his ideas about the mechanism that generates the bottom-trapped waves described in this article. The comments and suggestions of an anonymous reviewer are greatly appreciated.

REFERENCES

Auad, G., 1996: Circulation in the Santa Barbara Channel: Description, mass and heat budgets and forcing during 1984. Ph.D. thesis, Scripps Institution of Oceanography, UCSD, 241 pp. [Available from Scripps Institution of Oceanography Library, 9500 Gilman Dr., La Jolla, CA 92093.]

——, and M. C. Hendershott, 1997: The low frequency transport in the Santa Barbara Channel: Description and forcing. *Contin. Shelf Res.,* **17,** 779–802.

Brink, K. H., 1989: The effect of stratification on seamount-trapped waves. *Deep-Sea Res.,* **36**(6), 825–844.

——, and D. C. Chapman, 1985: Programs for computing properties of coastal-trapped waves and wind-driven motions over the continental shelf and slope. Tech. Rep. 85-17, 98 pp. [Available from Woods Hole Oceanogr. Inst., Woods Hole, MA 02543.]

——, and R. D. Muench, 1986: Circulation in the Point Conception Santa Barbara Channel region. *J. Geophys. Res.,* **91,** 877–895.

Dorman, C. E., and C. D. Winant, 1995: Buoy observations of the atmosphere along the west coast of the United States, 1981–1990. *J. Geophys. Res.,* **100,** 16 029–16 044.

Gunn, J. T., P. Hamilton, H. J. Herring, K. L. Kantha, G. S. Lagerloef, G. L. Mellor, R. D. Muench, and G. R. Stegen, 1987: Santa Barbara Channel Circulation Model and field study-final report. Dynalisis of Princeton, Reps. 92.1 and 92.2, 317 pp.

Kantha, L. H., A. F. Blumberg, H. J. Herring, and G. R. Stegen, 1985: The use and testing of a model for upper ocean dynamics. *The Ocean Surface,* Y. Toba and H. Mitsuyasu, Eds., D. Reidel Publishing Company, 547–552.

Koopmans, L. H., 1974: *The Spectral Analysis of Time Series.* Academic Press, 366 pp.

Lagerloef, G. S., and R. L. Bernstein, 1988: Empirical orthogonal function analysis of AVHRR surface temperature patterns in Santa Barbara Channel. *J. Geophys. Res.*, **93,** 6863–6873.

Limeburner, R., Ed., 1985: CODE-2. Moored array and large-scale data report. WHOI Tech. Rep. 85-35. CODE Tech. Rep. No. 38, 220 pp. [Available from Woods Hole Oceanographic Institution, Woods Hole, MA 02543.]

Merrifield, M., and R. T. Guza, 1990: Detecting propagating signals with complex empirical orthogonal functions: A cautionary note. *J. Phys. Oceanogr.,* **20,** 1628–1633.

Mooers, C. N. K., 1973: A technique for the cross spectrum analysis of pairs of complex valued time series, with emphasis on properties of polarized components and rotational invariants. *Deep-Sea Res.,* **20,** 1129–1141.

Rhines, P. B., 1970: Edge-, bottom and Rossby waves in a rotating, stratified fluid. *Geophys. Fluid Dyn.,* **1,** 273–302.

——, 1977: The dynamics of unsteady currents. *The Sea.* Vol. 6. Wiley Interscience, 189–318.

Thompson, R. O. R. Y., and J. R. Luyten, 1976: Evidence for bottom-trapped topographic Rossby waves from single moorings. *Deep-Sea Res.,* **23,** 629–635.

Wallace, J. M., and R. E. Dickinson, 1972: Empirical orthogonal representation of time series in the frequency domain. Part I: Theoretical considerations. *J. Appl. Meteor.,* **11,** 887–892.